Chaotic mixing efficiency in different geometries of Hele-Shaw cells

Aurélien Beuf, Jean-Noël Gence, Philippe Carrière, Florence Raynal *

Laboratoire de Mécanique des Fluides et d'Acoustique (UMR 5509), CNRS/Université de Lyon, École Centrale de Lyon/Université Lyon 1/INSA Lyon, 36 avenue Guy de Collongue, 69 134 Écully Cédex, France

ARTICLE INFO

ABSTRACT

Flows in Hele-Shaw cells are generally laminar, and can be in a first approximation considered as quasi-two-dimensional. Therefore, the only way to mix efficiently inside the cell is to generate a periodic flow and thus create chaos. Here we study the influence of the geometry of the cell on mixing efficiency: to this aim, we use three different geometries of the cell (circle, square and rectangle) and we numerically test them by using two protocols of mixing: the first protocol uses syringes, the second uses pumps. In a view of simplicity, this Hele-Shaw flow is modeled as two-dimensional, allowing us to analytically determine the velocity field corresponding to the different shapes. The results are then analyzed in terms of Poincaré sections (appearance, filling rate, and homogeneity), and the Lyapunov exponents are calculated. We numerically show that the rectangular geometry leads to a better mixing, but also that the aspect ratio of the rectangle plays unexpectedly no important role on mixing.

© 2009 Elsevier Ltd. All rights reserved.

1. Introduction

Microfluidic devices are widely used in nowadays' biotechnology, for applications ranging from transport of material in microchannels, sorting of cells, DNA analysis, etc. When chemical reactions come into play (e.g. in many such systems), efficient mixing is required in order to homogenize the solution, so as to favor the meeting of reactants. However, the Reynolds number of flows at the microscale are small, generally of the order of unity or smaller, so that Stokes flows should be commonly expected [1].

It is now well-known that chaotic advection is the best way to mix efficiently in laminar flows [2–5], all the more reason for microfluidic flows. Stroock et al. proposed a famous chaotic mixer adapted to microdevices, the so-called staggered herringbone mixer (SHM) [6], dedicated to mixing in microchannels. A typical microchannel has height and width of the order of 50–100 μm, and length of a few centimeters, i.e. two small dimensions and the third one large compared to the others. In a smooth channel the mixing of material between streams in the flow is purely diffusive, so that the length of channel required for mixing can be prohibitely long. The SHM consists in adding specific bas-relief structures (ridges) on the floor of the channel, leading to chaotic trajectories; the mixing length is therefore greatly reduced. In this paper, we deal with mixing in a different microfluidic configuration, the Hele-Shaw flows, where the height is small (typically 25–50 μm) and the length and width are "large", of the order of the centimeter.

Hele-Shaw flows can, in a first approximation, be considered as two-dimensional. In those conditions, the only way to achieve chaotic advection is to make the flow non-stationary; indeed, time-periodicity is enough.

We previously proposed two time-periodic protocols of mixing, one using two pairs of syringes, the other operating with pumps, and showed that they could exhibit chaotic trajectories in a *square* geometry [7,8]. Other chaotic protocols in a Hele-Shaw cell were proposed by two other teams: McQuain et al. [9] proposed a stirring protocol using pulsed pairs of syringe-driven source–sink systems in a *rectangular* chamber and tested it in a view of DNA chip hybridization: they showed that hybridization was significantly improved; then Stremler et al. [10,11] carried out the 2D mathematical analysis of mixing in their flow while the experimental analysis was done by Cola et al. [12]. Another work of importance was done by Hertzsch et al. [13] who showed that flows generated by pulsed source–sink pairs could be studied as linked twist maps; therefore they could relate the flow to mathematically precise notions of chaotic mixing, and proposed a new design to generate a well-mixed flow; they compared our protocol A, together with the protocol by Stremler et al., with their new protocol and showed that their protocol, which has mathematical properties in favor of better mixing, was indeed best in a *circular* geometry (see also Sturman et al. [14] for more details on the mathematical background).

The idea of this paper is not to compare all the protocols of stirring proposed in the literature for Hele-Shaw cells, but to test whether or not the *shape* of the chamber influences the quality of mixing. To this end, we use our two previous protocols [7,8], which have been shown to exhibit very different mixing abilities. Fluid flow is created thanks to four vertical pipes located near

* Corresponding author.
  E-mail address: florence.raynal@ec-lyon.fr (F. Raynal).

Nomenclature

c	distance from the center to a corner (square and rectangle)	w	parameter measuring the distance between a point and the center
D	diffusion coefficient	$w_c(z)$	complex velocity field at complex point z
h	height of the Hele-Shaw cell	x, y	coordinates in a plane
h_K	Kolmogorov entropy	z	complex coordinate, $z = x + iy$
i	natural base of complex numbers	α	dimensionless pulse volume
$K(k)$	Jacobi function	β	parameter for the position a source with respect to the center
L	side of a square chamber		
$P_{t=t_0}$	Poincaré section for initial time t_0	γ	aspect ratio parameter for the rectangle
q	flow-rate	λ	Lyapunov exponent
R	radius of the circular cell	μ	fraction of covered area
S	surface of the horizontal section of the cell	$\tau(w)$	function for the time needed for a point to go from source to sink
t	time		
T	period of the flow-field	ξ	intermediate parameter
T^*	dimensionless period of the flow-field		

the corners, which inject or extract fluid, and therefore act as sources or sinks. Indeed, those protocols can be considered as variants of the pulsed source–sink chaotic mixer first proposed by Jones and Aref [15].

1. The first protocol (called protocol A in the following) relies on periodic injection of fluid thanks to four reversible syringes: during one period T, four steps of same duration occur (Fig. 1(a)).
2. The second protocol (protocol B) operates with two monodirectional pumps switched alternately. For this protocol, only two steps of same duration occur during T (Fig. 1(b)).

In all the following, like in our previous works [7,8], the flow rate q, the height h, and the horizontal section S are chosen such that $q/hS = 0.18 \text{ s}^{-1}$; the shape of the cell is whether a circle, a square of side L (like in our previous works), or a rectangle of lateral sides γL and $L\gamma$, where we took different values for $\gamma > 1$, so that the total surface is, in all cases, equal to S.

2. Numerical tools

2.1. Numerical model

The velocity field is modeled as purely *two-dimensional* in a first approximation, using the depth-averaged horizontal velocity field,

which, in a Hele-Shaw flow, satisfies the Euler equation. Indeed, the aim of this work is to test the influence of the shape of the domain, and for this purpose such a 2D model is much more flexible than the calculation of the whole 3D flow, for which a change of geometry requires a new computational grid, together with heavy calculations. In our case the flow between a source and a sink is calculated *analytically* in a *circular* geometry using the Milne-Thomson theorem [16]. It is then very easy to obtain the flow in the *square* or *rectangular* geometry using a Schwarz–Christoffel transformation [16]. All the analytical details of the 2D calculations are given in Appendix A. The streamlines obtained with our model for a source–sink flow are shown in Fig. 2 for different geometries of the chamber. The trajectories are calculated thereafter using a standard fourth order Runge–Kutta integration. Like in the 3D simulations, our calculations have been performed without taking into account molecular diffusion.

In our 2D model, we impose that a particle entering in a sink reenters the flow domain *on the same streamline*. The underlying aim is to avoid adding artificial mixing other than that imposed by chaotic advection. With this hypothesis, a fluid particle at a given location at the end of an injection/extraction stage of protocol A, which is swallowed inside a pipe during the next stage comes back at exactly the same location when the sink is turned again into a source. In a laboratory experiment or in the 3D calculations, however, the flow-field is not expected to be *exactly* zero in the
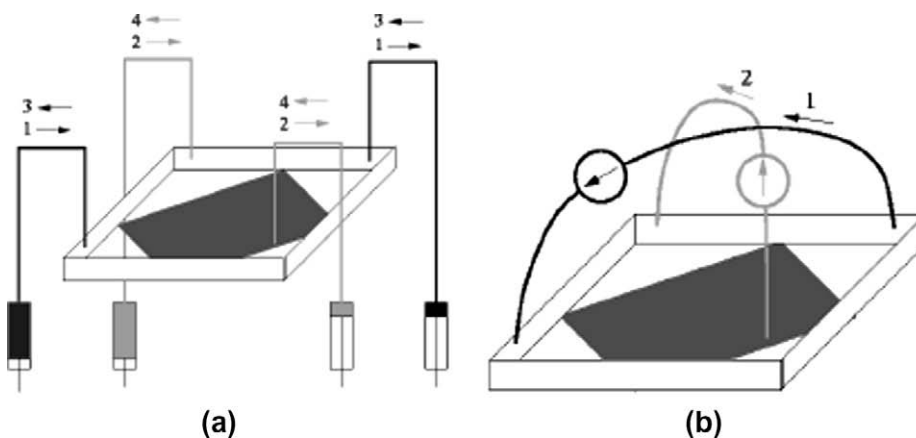
Fig. 1. (a) Alternating injection scheme for protocol A. Each quarter-period step of the protocol involves two opposite syringes (the black ones in steps 1 and 3, the grey ones in steps 2 and 4), the two other ones being inactive. (b) Same for protocol B. Each half-period step of the protocol involves one of the pumps, the other being inactive. One pump always pushes the fluid in the same direction, or else is inactive. *Note*: the DNA chip is symbolized by the central black square.
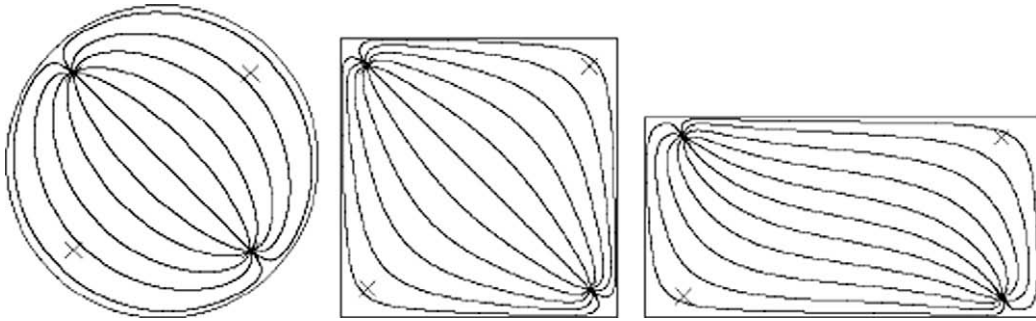
Fig. 2. Streamlines for a source–sink flow in the different geometries of the chamber.

non-active pipes: because of the flow inside the cell, friction causes in those pipes the formation of a large sequence of eddies, each exponentially weaker than its predecessor as height grows [17,18]. Of course this effect is very weak; but since the streamlines are very tight inside an active pipe, a change in a fluid particle location during the "inactive" stage, leads the fluid particle to come back *nearly*, but not *exactly* at the same location. Even though this effect is small, it may affect regular regions visible on the 2D Poincaré sections after integration of fluid particle trajectories on very long times, as we will see later. Therefore, because our 2D model neglects the weak mixing inside the non-active pipes, it is likely to mix less than in reality.

Note that *long time integration of trajectories* is also more easily available with the 2D model than with a 3D flow on a computational grid, since the probability that a fluid particle ends on a boundary is very low in the former case: first the flow-field is known analytically, and therefore satisfies exactly the incompressibility constraint, and second the velocity, which is a solution of the Euler equation, is not zero on the boundaries.

2.2. Correspondence between parameters from different authors

It is clear that the efficiency of mixing does not depend on the value of the Reynolds number inside the pipes and inside the chamber, as long as it remains small. Therefore, *for a given geometry and a given protocol*, the important non-dimensional parameter is the dimensionless pulse volume α:

$$\alpha = \frac{qT}{hS}, \qquad (1)$$

which represents the volume of fluid displaced during one period compared to the volume of the chamber. Although α is defined for the 3D flow, one can easily switch from volumes to surfaces by dividing by the – constant – height h of the chamber. Therefore, α can be used identically as its 2D equivalent, the dimensionless pulse area, equal to the surface of fluid displaced during one period compared to the surface of the chamber.

In a view of comparison with our previous works where we used the dimensional period of the flow T instead of α, note that those two parameters are linked by the relation $\alpha = 0.18T$ (T in s) with our set of parameters.

While Stremler and Cola also used α, Hertzsch et al. used a non-dimensional period – denoted here T^* – defined as $T^* = qT/2\pi a^2$, where the distance between the source and the sink is equal to $2a$; in their simulations, the radius of the circular chamber is equal to R, chosen as $R = 2a$, which leads to the relation $\alpha = T^*/2$.

2.3. Tools of chaos

Mixing efficiency is then analyzed with the usual tools of chaos: Poincaré sections and Lyapunov exponents. In a time-periodic flow,

the Poincaré section of a given trajectory is obtained by plotting on the same graph all the positions of the initial point taken every period. A good mixing is obtained when the Poincaré section of a single trajectory covers the whole surface, in the most homogeneous way and the smallest period possible.

Mixing can also be analyzed quantitatively using the Lyapunov exponent λ, expressed in s^{-1}, which measures the asymptotic exponential stretching between two nearby trajectories (rate of separation). Classically in a 2D incompressible flow, the sum of the two Lyapunov exponents is zero, so that we only need to calculate the largest Lyapunov exponent (in opposition to our previous works in 3D flows where we determined the three Lyapunov exponents [19]). We check that the calculation is sufficiently converged by taking different initial points inside the stochastic region; the simulation is stopped when all Lyapunov exponents have converged towards the same value.

In the square and rectangular geometry, it is also possible to calculate the "filling rate" of the Poincaré section, i.e. the fraction of surface covered, so as to obtain a quantitative rather than visual information (for a discussion on how to measure the filling rate of an ensemble of points, see [20]). We can therefore investigate the use of the topological or Kolmogorov entropy h_K through the same estimation as Stremler and Cola [11], as the product of the fraction of the phase space covered by a *single* chaotic trajectory multiplied by the corresponding Lyapunov exponent (see [21, Section *Definitions and basic concepts*, p. 305]). Mixing is supposed to be all the more efficient as the topological entropy is high.

2.4. Validation of the 2D model

It is important first to validate the 2D model properly. Indeed, our 2D model uses the *depth-averaged* horizontal velocity field, whereas the horizontal velocity profile is almost everywhere parabolic. This implies that a fluid particle located at middle-height moves faster than what we compute, while another one located for example near the bottom can be much slower. Therefore, we could fear some important discrepancies between our 2D results and our 3D calculations.

Note also that, since a Poincaré section accumulates the positions of a fluid particle after each period, and since a fluid particle can change depth, the 3D Poincaré section is a 3D set of points, and a regular region is likely to be hidden by points located above and below this region (corresponding to points with different velocities), which is not possible in the 2D case.

In Fig. 3 are compared 3D (left) and 2D (right) Poincaré sections, together for protocol A for three values of α, and for protocol B for a very small α – the comparison for protocol B and large values of α is of little interest, since points are almost randomly spread in the whole domain.

Concerning protocol B (Fig. 3(a) and (b)), the matching is very good. For protocol A $\alpha = 0.36$ (Fig. 3(c) and (d)), the situation is also
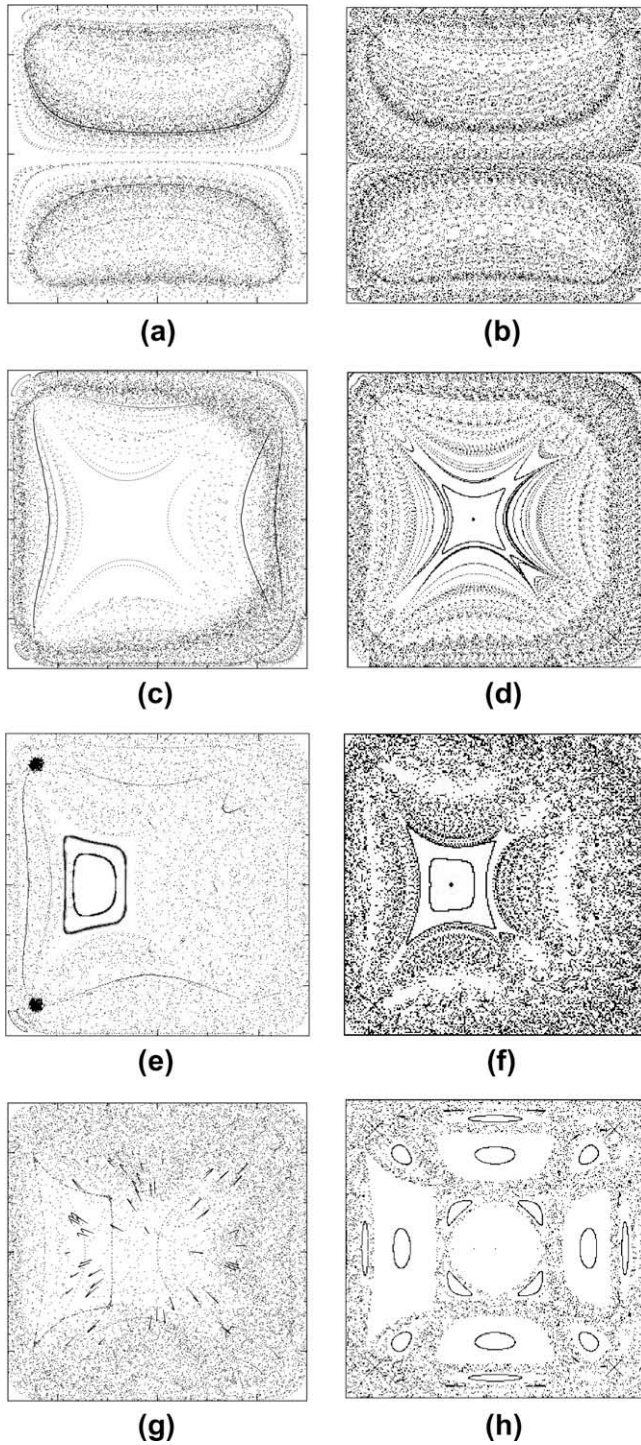
Fig. 3. Comparison between Poincaré sections with 3D velocity flow (left) and 2D model velocity flow (right). (a) and (b) Protocol B, $\alpha = 0.09$; (c) and (d) protocol A, $\alpha = 0.36$; (e) and (f) protocol A, $\alpha = 0.72$; and (g) and (h) protocol A, $\alpha = 1.8$.

very similar: the peripheral region of the domain, more dense, corresponds to a chaotic zone, while the region inside is a nearly regular region For protocol A, $\alpha = 0.72$ (Fig. 3(e) and (f)), the chaotic area (area full of points) and large regular island (empty area or area having "elliptical trajectories") have comparable shape, size, and location. The regular islands located around the large one are very thin, and therefore can hardly be detected in the 3D calculations, as explained before.

For larger values of α (for instance $\alpha = 1.8$ in Fig. 3(g) and (h)), some very large regular regions are present in the 2D case, that

are not visible in the 3D case. At first sight, the correspondence may appear quite bad. However, a careful analysis shows that the 2D Poincaré section is indeed informative in the present case: let us consider the large island which repeats identically at three occurrences in the section (bottom, right and top, denoted by regions A, B and C in Fig. 12). A point in one of these islands is in fact a periodic point, and enters and leaves the different pipes eight times before it comes back to its initial position seven periods later, see Appendix B (we remind that a complete period is made of four stages). As explained before, some mixing occurs inside the pipe, even when non-active. This explains why these zones are not visible in the 3D section.

The trapezoidal-shaped island on the left is, on the other hand, never swallowed inside a pipe, but moves in the domain with time (this is indeed the same regular region as the large island seen in Fig. 3(f) and at the middle of Fig. 3(d), which grows in size and is slightly displaced towards the left with increasing period). Therefore, we should expect a fluid particle trapped inside this region to remain there for many periods before leaving; this is indeed the case, as can be seen in Fig. 3(g), where a curve corresponding to the trapezoidal area is visible. It is also noticeable that both this region and the central region are less visited than the rest of the domain (less points in the section), in accordance with the corresponding regular regions in the 2D section (Fig. 3(h)). Therefore, even in this case, we recover special features of the 2D section in the 3D calculations. Note that in a real experiment, because of molecular diffusion, the mixing will be even more rapid than in the 3D calculations.

Since we present Lyapunov exponents as a quantitative tool, we could wonder whether the hypothesis of a quasi-2D flow does not alter *quantitatively* this parameter. In Fig. 4 are presented with symbols the Lyapunov exponents obtained with our model flow versus the dimensionless pulse area α. As a view of comparison are plotted with lines the results obtained with the full 3D calculations in a square chamber [8]; the dotted line corresponds to protocol A and is to be compared with the empty square symbols (2D flow), while the solid line (protocol B) shall be compared with the full square symbols: somewhat surprisingly, the comparison shows almost perfect matching, except for very small values of α, when the horizontal dispersion by the flow is weak, so that 3D effects cannot be neglected anymore.

We therefore conclude that this 2D velocity field model is adapted for a complete study of the problem.
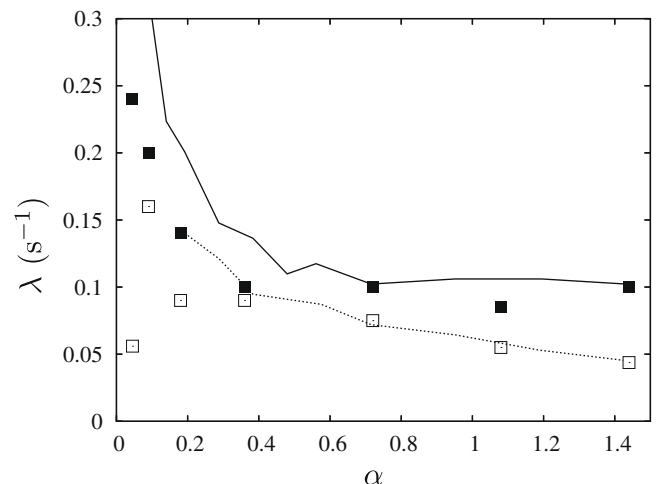
Fig. 4. Comparison of Lyapunov exponents from 2D and 3D calculations in the squared geometry. ($\square$) protocol A, 2D calculations, ($\blacksquare$) protocol B, 2D calculations. The lines correspond to the Lyapunov exponents obtained in our previous work with complete 3D calculations [8]: ($\cdots\cdots$), protocol A; (—) protocol B.

3. Results

3.1. Poincaré sections and Lyapunov exponents

Poincaré sections are usually the most straightforward tools for characterizing chaos, because of the visual information they provide. In Figs. 5 and 6 are shown Poincaré sections of protocols A and B, respectively, for three values of α, namely $\alpha = 0.18$, $\alpha = 0.72$ and $\alpha = 1.8$ (corresponding to the periods $T = 1$ s, $T = 4$ s and $T = 10$ s from our previous work).

The circular, square or rectangular domains have been plotted with the same area so as to be able to compare them visually – in the case of the circle, although this is not obvious, we indeed have $S = \pi R^2 = L^2$, with R the radius of the circle, which implies that the diameter is $2R/L = \sqrt{4\pi} \simeq 1.13$. As expected [8], we recover with our 2D model that mixing is much more efficient with protocol B compared to protocol A in the square geometry; this result can obviously be extended to different geometries of the chamber.

A more surprising result is the influence of the geometry of the chamber: the fact is not straightforward concerning protocol B, since mixing is quite good, even if not *perfect* in the square geometry (some small regular regions still persist, Fig. 6(e) and (h), but which are much too small to be seen in a 3D computation or an experiment). However, mixing is as good in the rectangle as in the circle. The results are much more striking concerning protocol A, since mixing is not very good, neither in the circle nor in the square: the very robust regular region for protocol A, $\alpha = 0.72$, seen in the 3D or 2D calculations (Fig. 3(e) and (f)) of the *square* geometry, also present in the circular geometry (Fig. 5 (d)), has totally disappeared in the *rectangular* geometry. For the largest value of α studied, $\alpha = 1.8$ (also protocol A), the very large islands seen in the circle and the square (Fig. 5(g) and (h)) have a much more limited extent in the rectangular geometry. In fact, we performed many 2D calculations, but we could hardly find cases with regular regions (except for protocol A and large values of α, where a fluid particle at the center is always swallowed into a sink after a source/sink phase, and always comes back to its initial position when the sink is turned into a source again) – although we will show two particular cases (one for each protocol) where some small islands are indeed still present.
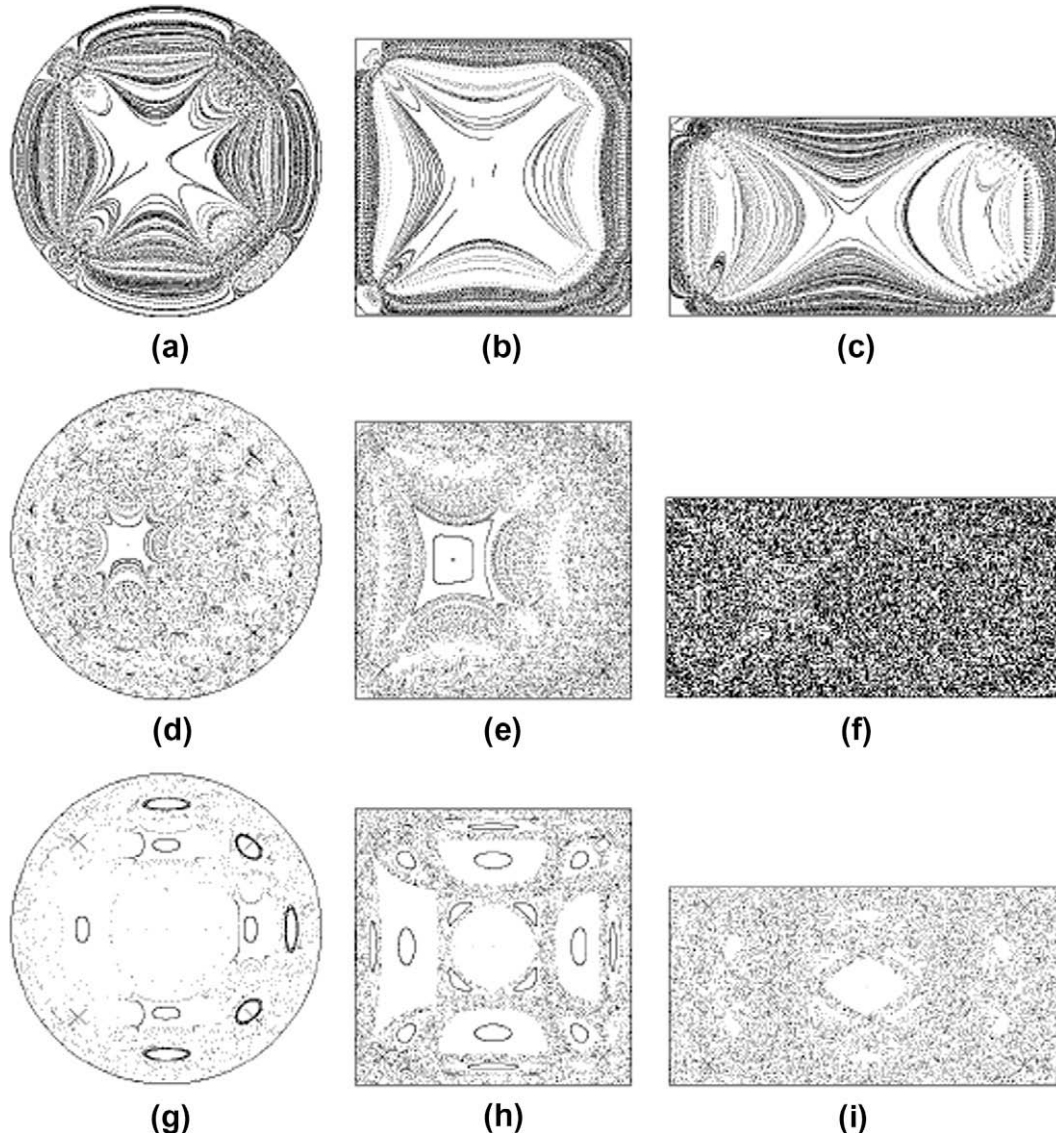
Fig. 5. Poincaré sections: comparison circular/squared/rectangular geometry of the chamber with protocol A (syringes) for $\alpha = 0.18$ (top), $\alpha = 0.72$ (middle), and $\alpha = 1.8$ (bottom).
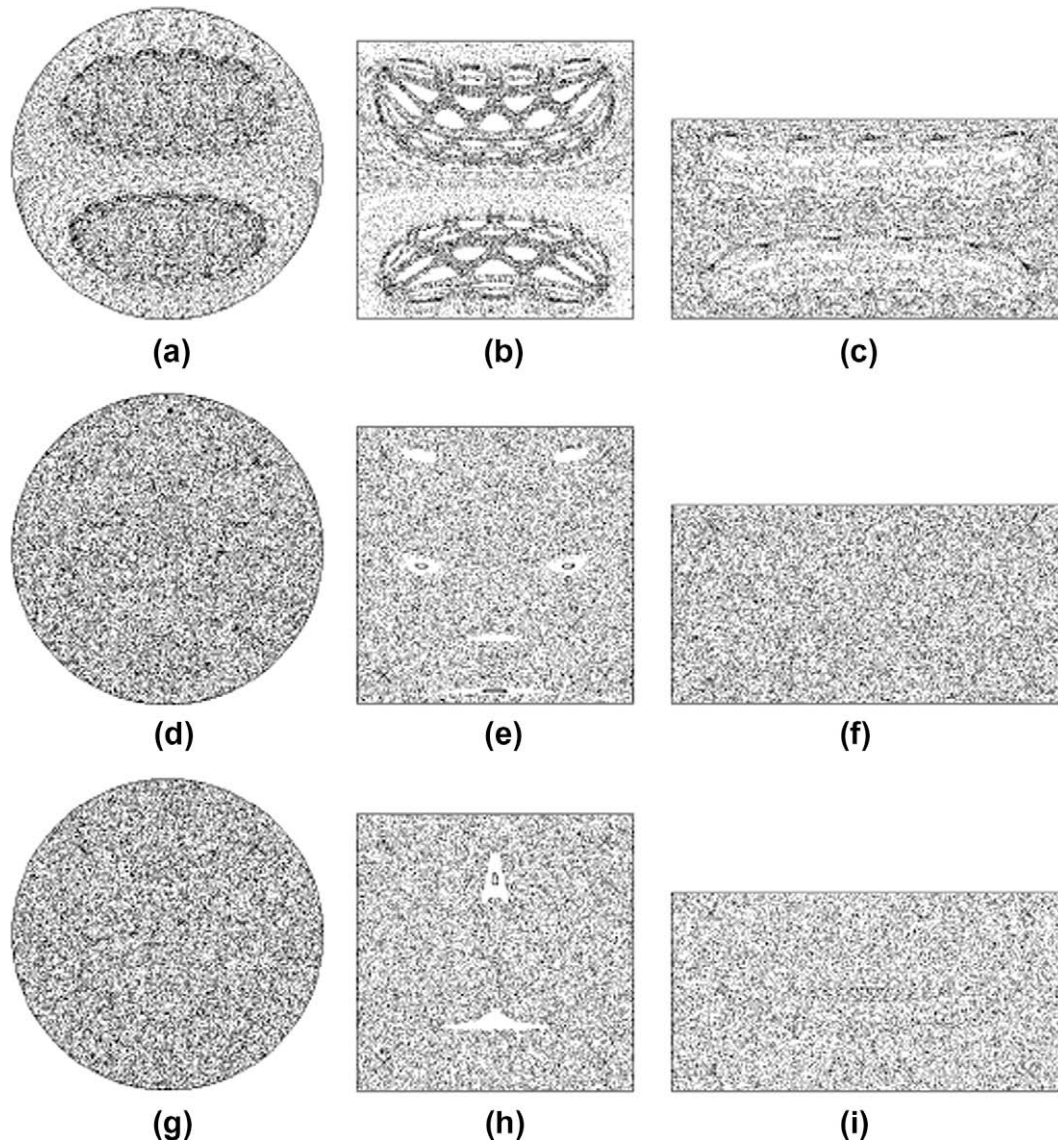
Fig. 6. Poincaré sections: comparison circular/squared/rectangular geometry of the chamber with protocol B (pumps) for $\alpha = 0.18$ (top), $\alpha = 0.72$ (middle), and $\alpha = 1.8$ (bottom).

We wanted to know whether the fact that mixing was best in the rectangular geometry was robust with respect to the aspect ratio of the rectangle, or else if the 2:1 aspect ratio was a particular case: in Fig. 7 are shown different Poincaré sections, for the same case protocol A, $\alpha = 0.72$, from the square geometry to rectangles with aspect ratios ranging from 3:2 to 4:1. In all rectangular Poincaré sections, the regular island is not present (although all of them present the same star-shaped region where the repartition of points is not completely homogeneous), as if the topology of chaos did depend much on the geometry (circular, square or rectangular) but not on the aspect ratio of the rectangle either. A similar conclusion can be drawn when looking at Fig. 8, where the small regular islands seen both for protocol A with $\alpha = 1.44$ or protocol B with $\alpha = 1.8$ are topologically similar in the 2:1 and 3:1 rectangles.

We could calculate the Lyapunov exponent for both protocols and each geometry (circle, square, rectangle 2:1). The results are shown in Fig. 9, where the black symbols represent protocol B, while the empty symbols are for protocol A: surprisingly, although the Lyapunov exponent depends much on the protocol, it seems not to depend much on the geometry – it is slightly above in the

rectangular case for $\alpha < 1.44$, but is also slightly below for $\alpha > 1.44$, although the Poincaré sections always show a much better chaos. Moreover, the maximum of the Lyapunov exponent (the smallest value of α tested, $\alpha \simeq 0.045$ for protocol B, and $\alpha \simeq 0.09$ for protocol A) is not representative of a good mixing: the stirring is important, but in a restricted chaotic domain. We can conclude that the Lyapunov exponent is quite robust with respect to the protocol; however, as expected the Lyapunov exponent is not the relevant quantity to decide between different geometries.

3.2. Topological entropy

As mentioned at the end of the previous section, there is a need to find a different *quantitative* parameter which could help decide on whether the rectangular geometry indeed leads to more efficient mixing than square or circular shapes. We propose to try to use the topological entropy, calculated as the fraction of surface covered *by a single trajectory*, multiplied by the corresponding Lyapunov exponent [21]. As seen before, the Lyapunov exponent depends poorly on the geometry of the chamber, so that the
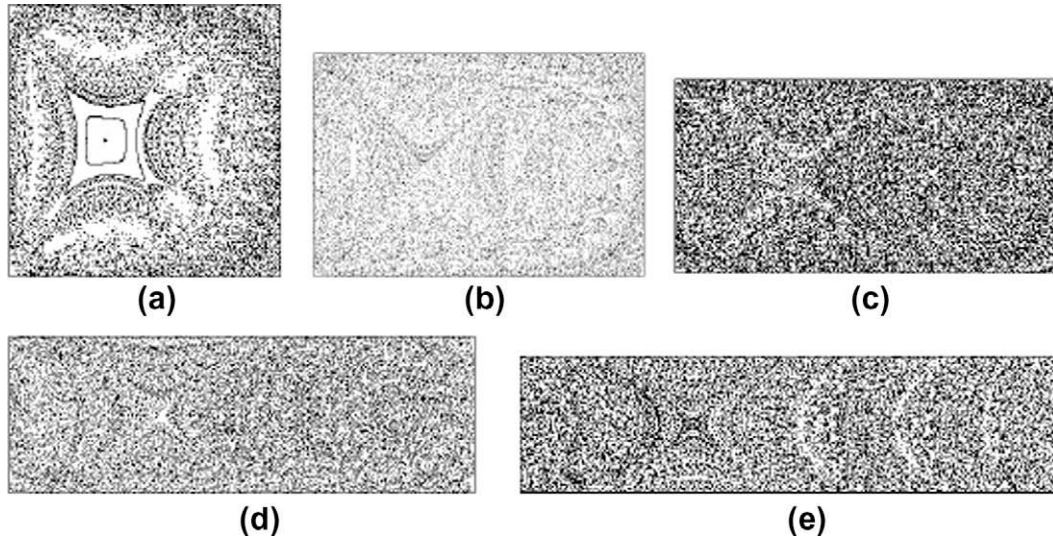
Fig. 7. Comparison of different aspect ratios from squared to rectangular geometry, for protocol A, α = 0.72: (a) square; (b) rectangle 3:2; (c) rectangle 2:1; (d) rectangle 3:1; and (e) rectangle 4:1.
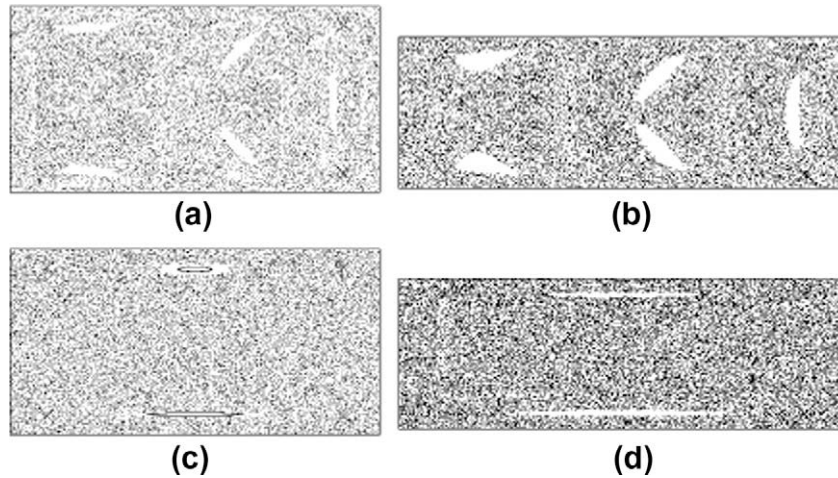
Fig. 8. Poincaré sections: comparison 2:1/3:1 rectangular chamber for protocol A with α = 1.44 ((a) and (b)), protocol B with α = 2.52 ((c) and (d)). We chose in purpose cases where small regular regions did exist.

topological entropies for different geometries should follow more or less the behavior of the filling rate of the sections. However, for very small values of α the filling rate is low, even for protocol B, while for the same protocol the Lyapunov exponent is a decreasing function of α (Fig. 9); therefore we could wonder whether the product of the filling rate by the Lyapunov exponent would present a maximum that could be interpreted as an indicator of the optimum of α.

In Fig. 10(a) is shown the filling rate of the Poincaré section as a function of the dimensionless pulse area α, for both protocols in the square and rectangle 2:1, calculated using a single fluid particle followed for 10,000 periods. In accordance with the aspect of the Poincaré section, the filling rate is nearly always higher in the rectangular geometry. When multiplied by the Lyapunov exponent, the topological entropy is obtained, as shown in Fig. 10(b): concerning protocol B, no maximum was found, neither in the square nor in the rectangle; as for the Lyapunov exponent, the quantity is decreasing with increasing α, greater for the rectangle than for the square for α < 1.44, and lower thereafter. It is clear though that the smallest values of α are not those associated with the best chaos, as seen in Fig. 6(a)–(c) for protocol B, α = 0.18. In the case

of protocol A, however, a maximum exists for the topological entropy, located at $\alpha \simeq 0.36$ for the square (which corresponding Poincaré section can be seen in Fig. 3(d)), and $\alpha \simeq 0.72$ for the rectangle (Fig. 5(f)). This may indeed correspond to an optimal period for mixing in the rectangle, but inspection of Fig. 3(d) reveals that this is not obvious in the case of the square. Moreover, the topological entropy does not differ much from square to rectangle, although the filling rate proves that chaos is much more extended in the rectangle for this protocol. Therefore, the use of the topological entropy, even if giving some interesting quantitative information, is not totally convincing.

4. Discussion

The *protocols* have approximately the same symmetries for the different geometries: in the case of protocol A the equations of the trajectories in the 2D or 3D flow are invariant under the change of variables $t \to -t$, $x \to x$, $y \to -y$, $z \to z$. This implies that the Poincaré sections $P_{t=0}$, corresponding to the accumulated periodic positions of particles, starting at $t = 0$, are invariant un-
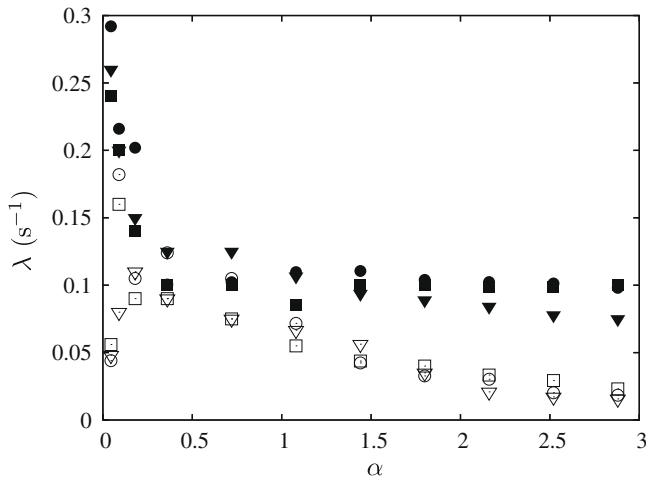
Fig. 9. Lyapunov exponent λ. Full symbols: protocol B; empty symbols: protocol A. Squared symbols: squared geometry; circles: circular geometry; triangles: rectangular geometry. Therefore, ($\triangledown$) rectangle + protocol A, ($\blacktriangledown$) rectangle + protocol B, ($\square$) square + protocol A, ($\blacksquare$) square + protocol B, ($\circ$) circle + protocol A, and ($\bullet$) circle + protocol B.
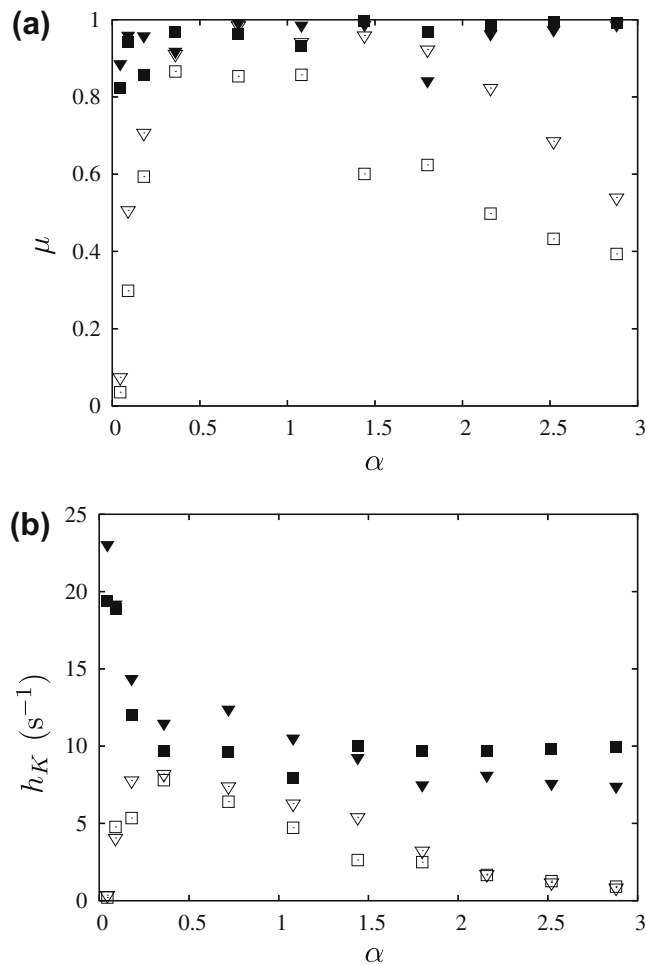
Fig. 10. (a) Filling rate μ and (b) topological entropy $h_K = \mu \times \lambda$ (in s^{-1}) as a function of α. Full symbols: protocol B; empty symbols: protocol A. Squared symbols: squared geometry; triangles: rectangular geometry. Therefore, ($\triangledown$) rectangle + protocol A, ($\blacktriangledown$) rectangle + protocol B, ($\square$) square + protocol A, and ($\blacksquare$) square + protocol B.

der reflection in the plane $y = 0$. In the square, a translation in time $t \to t + T/4$ leaves the flow unchanged after rotation of an-

gle $-\pi/2$, and the Poincaré section $P_{t=T/4}$ is obtained from the Poincaré section $P_{t=0}$ by a rotation of angle $-\pi/2$; this is of course not true anymore in the rectangle, but if now we consider the translation in time $t \to t + T/2$, two consecutive rotations of angle $-\pi/2$ are equivalent to a rotation of angle π, which is also a point symmetry. One can check that this last symmetry is also present in the rectangular geometry. In the case of protocol B, the invariance of particle trajectories under $t \to -t$, $x \to -x$, $y \to y$, $z \to z$ implies that the Poincaré sections $P_{t=0}$ are invariant with respect to reflection in the plane $x = 0$. The translation in time $t \to t + T/2$ leaves the flow unchanged after reflexion in the plane $y = 0$, which implies that the Poincaré section $P_{t=T/2}$ is, in all the geometries studied here, obtained from the Poincaré section $P_{t=0}$ by reflection in y. Therefore, the improvement of results seen in the Poincaré sections in the rectangle does not result from a breaking of symmetry in the combined effect of protocol and new geometry.

Recently, Hertzsch et al. showed that flows generated by source–sink pairs could be studied as "Linked Twist Map" (LTM) [13]. The central idea of their paper was to construct crossed periodic flows having properties as close as possible to those of an ideal model, i.e. (I) crossing of streamlines as orthogonal as possible, and (II) velocity field as close to monotonous as possible. We propose to test properties (I) and (II) on our different geometries.

In Fig. 11 are shown superimposed streamlines for the two source–sink pairs for the different geometries. In all cases the streamlines are close to tangential near the boundaries. In the central region, however, the greatest transversality is found in the circular and square geometry, where streamlines are close to orthogonality, whereas mixing is much more efficient in the rectangle. In the case of the rectangle 3:1 (Fig. 11(d)), the situation is even worse, since the streamlines in the central region are nearly tangential. Loss of transversality works here in favor of mixing, rather than against it.

We now try to find out whether the flow-field in the rectangular geometry is more monotonous than in the square or the circle. It is quite difficult to compare velocity profiles since the flow is not unidirectional, but we can compare the time needed to go from the source to the sink on each streamline instead. To this end, let us come back to Fig. 2 where streamlines of a source–sink pair are shown for the different geometries: for a given phase with a source–sink pair, let us consider the segment joining the two other corners, that we will chose as our axis of reference. We graduate it from $-c$ to $+c$, where c is the distance from the center to one corner, and we denote by $\tau(w)$ the time needed to join the sink starting from the source ($-c \leqslant w \leqslant c$). In the circle and the square, the streamlines are symmetric with respect to any line joining a source and a sink; therefore $\tau(w)$ is a symmetric function, and is absolutely not monotonic. In the off diameter source–sink model proposed by Hertzsch et al. in a circle [13], $\tau(w)$ is dissymmetric, and much closer to a monotonic function. In the rectangle, however, although the two symmetries with respect to the lines joining a source–sink pair do not hold, the streamlines are clearly symmetric with respect to the center. This implies that $\tau(w)$ is, as for the circle or the square, a symmetric function, therefore not monotonic either.

We conclude that the only reason for the improvement of mixing in the rectangular geometry is the loss of symmetry of the streamlines themselves. The line joining the source and the sink is no more a streamline of the corresponding flow. Instead, the streamline that goes through the center point wanders from one side of this line to the other, all the more as the rectangle has a large aspect ratio. This last point could explain also why, although superimposed streamlines are even more tangential when the aspect ratio of the rectangle is increased, mixing remains good, and the Poincaré section mostly unchanged.
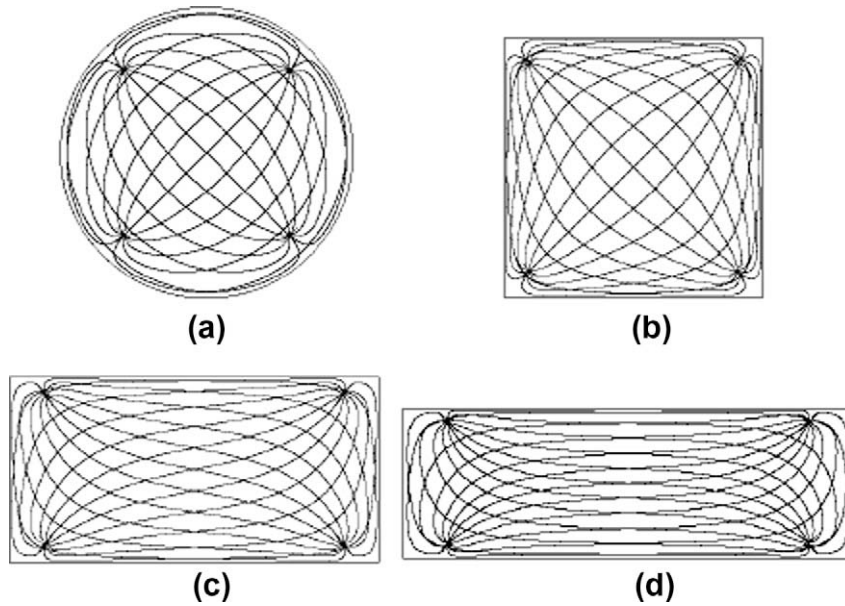
Fig. 11. Superpositions of streamlines created independently by the two source–sink pairs.

5. Summary and conclusion

In this paper, we tested the influence of the geometry of Hele-Shaw cells on the quality of chaotic mixing, using two different mixing protocols that relied on chaotic advection. In a view of fast design, we used a 2D model consisting in the depth-average velocity field: it could be easily calculated analytically for a source–sink flow, first in a circle, and in a square or rectangle thereafter with a Schwarz–Christoffel transformation. The model was validated using various Poincaré sections in a square, that qualitatively matched our previous 3D calculations. As a more quantitative tool, 2D and 3D Lyapunov exponents were also compared, with good agreement. We thus could show that mixing in the rectangular geometry was nearly always best (better filling of the Poincaré sections, usually higher Lyapunov exponents, higher topological entropy), whatever the protocol used. The result did not depend much on the aspect ratio of the rectangle.

We tried to find out whether the improvement in mixing in the rectangle could be relied to loss of symmetry in the protocols compared to squared or circular geometry, with no success. Then we searched for properties proposed by Hertzsch et al. in order to approach more ergodic systems, namely increase in transversality of superimposed streamlines, and monotonicity of the velocity profile, but this study revealed that the profile was no more monotonic in the rectangle than in the square or the circle, and that, on the contrary, the streamlines were even less perpendicular. We then concluded that the only reason for this improvement was the loss of symmetry in the streamlines for a source–sink flow in the rectangular geometry: whereas in the square or the circle the streamlines have two axes of symmetry, in the rectangle only a point symmetry remains. More specifically, the straight line joining the source and the sink is no more a streamline in the rectangle.

This improvement in mixing in the rectangular geometry is all the more important in practice as a straightforward application of mixing in Hele-Shaw cells is the enhancement of reliability of DNA chips technology, and that most DNA chips are manufactured on microscope lids, which have a rectangular shape.

Appendix A. Velocity field

In order to obtain the flow in the squared or rectangular domain, the velocity field is first easily calculated in a circular chamber using the Milne-Thomson theorem. Let $v_x(x, y)$ and $v_y(x, y)$ the components of the velocity-field at point (x, y). The complex velocity-field $w_c(z)$ is

$$w_c(z) = v_x(x, y) - i \; v_y(x, y), \tag{2}$$

where i is the natural base of complex numbers, defined as $i^2 = -1$, and $z = x + iy$. In a circular cavity of radius R, the flow of rate q created by one pair source/sink in opposition at length βR from the center of the cavity is:

$$w_c(z) = \frac{q}{2\pi} \left(\frac{1}{z + \beta R} - \frac{1}{z - \beta R} + \frac{1}{z + R/\beta} - \frac{1}{z - R/\beta} \right). \tag{3}$$

Then a Schwarz–Christoffel function g, adapted to the transformation of a circle into a square or rectangle, is calculated [16,22]: let k and ξ be solutions of equation:

$$\frac{K(k)}{a} = \frac{K\left(\sqrt{1 - k^2}\right)}{b} = \frac{\xi}{2}, \tag{4}$$

where K is a Jacobi function [23] and a and b the lengths of sides of the squared (or rectangular) cavity. Then g is defined as:

$$g(z) = \frac{\text{sn}(\xi z/2, k)\text{dn}(\xi z/2, k)}{\text{cn}(\xi z/2, k)}, \tag{5}$$

where sn, cn and dn are elliptical functions [23].

Finally, the velocity field $w_r(z)$ inside a square (or rectangular) shape is defined as:

$$w_r(z) = w_c(g(z)) \times \frac{dg}{dz}. \tag{6}$$

Appendix B. Study of the period-7 periodic point in Fig. 3(d)

We describe here briefly how the regular region that wanders in the whole squared domain in Fig. 3(d) returns to its initial position after 7 periods, while only three identical regions are seen on the
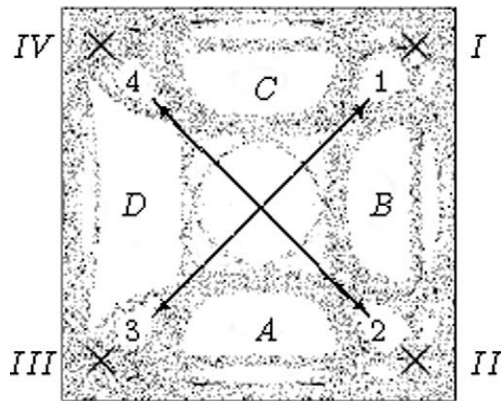
Fig. 12. Sketch of the velocity field for the Poincaré section corresponding to protocol A, $\alpha = 1.8$ in the square: during stage 1 (respectively, 2, 3 or 4), the sink is the hole located at cross *I* (respectively, *II, III* or *IV*), the source is the hole located at the cross at the opposite corner.

Poincaré section. Consider Fig. 12: crosses *I, II, III* and *IV* represent the pipes. Protocol A consists in four stages per period; during the first one, denoted by stage 1 (respectively, 2, 3 and 4), the active couple is *I* and its opposite hole, the sink being *I* (respectively, *II, III* and *IV*). For this set of parameter, a fluid particle located in regular region *A* (respectively, *D*) is mapped into *B* (respectively, *C*) during this stage, and a fluid particle located at *B* or *C* is swallowed into pipe I. We remind that a fluid particle swallowed into a pipe comes back at the same location when the sink is turned into a source again. We can therefore follow a fluid particle initially in regular region *A*, knowing that each period is composed of the four stages 1, 2, 3 and 4.

First period: $A \rightarrow B \rightarrow$ pipe *II* $\rightarrow$ pipe *II* $\rightarrow B$.
Second period: $B \rightarrow$ pipe *I* $\rightarrow$ pipe *I* $\rightarrow B \rightarrow C$.
Third period: $C \rightarrow$ pipe *I* $\rightarrow$ pipe *I* $\rightarrow C \rightarrow$ pipe *IV*.
Fourth period: pipe *IV* $\rightarrow$ pipe *IV* $\rightarrow C \rightarrow D \rightarrow$ pipe *IV*.
Fifth period: pipe *IV* $\rightarrow$ pipe *IV* $\rightarrow D \rightarrow$ pipe *III* $\rightarrow$ pipe *III*.
Sixth period: pipe *III* $\rightarrow D \rightarrow A \rightarrow$ pipe *III* $\rightarrow$ pipe *III*.
Seventh period: pipe *III* $\rightarrow A \rightarrow$ pipe *II* $\rightarrow$ pipe *II* $\rightarrow A$.

Therefore, there are indeed seven identical regular regions in the Poincaré section, three of which are visible in the section, two inside pipe *IV*, two others inside pipe *III*.

References

[1] H.A. Stone, A.D. Stroock, A. Ajdari, Engineering flows in small devices: microfluidics toward lab-on-a-chip, Annu. Rev. Fluid Mech. 36 (2004) 381–411.
[2] H. Aref, Stirring by chaotic advection, J. Fluid Mech. 143 (1984) 1–21.
[3] S. Wiggins, Global Bifurcations and Chaos: Analytical Methods, Springer, New York, 1988.
[4] J.M. Ottino, The Kinematics of Mixing: Stretching, Chaos and Transport, Cambridge University Press, New York, 1989.
[5] Valérie Toussaint, Philippe Carrière, Florence Raynal, A numerical Eulerian approach to mixing by chaotic advection, Phys. Fluids 7 (11) (1995) 2587–2600.
[6] Abraham D. Stroock, Stephan K.W. Dertinger, Armand Ajdari, Igor Mezic, Howard A. Stone, George M. Whitesides, Chaotic mixer for microchannels, Science 295 (5555) (2002) 647–651.
[7] F. Raynal, F. Plaza, A. Beuf, Ph. Carrière, É. Souteyrand, J.-R. Martin, J.-P. Cloarec, M. Cabrera, Study of a chaotic mixing system for DNA chip hybridization chambers, Phys. Fluids 16 (9) (2004) L63–L66.
[8] F. Raynal, A. Beuf, F. Plaza, Julian Scott, P. Carriere, M. Cabrera, J.-P. Cloarec, É. Souteyrand, Towards better DNA chip hybridization using chaotic advection, Phys. Fluids 19 (1) (2007) 017112.
[9] M.K. McQuain, K. Seale, J. Peek, T.S. Fisher, S. Levy, M.A. Stremler, F. Haselton, Chaotic mixer improves microarray hybridization, Anal. Biochem. 325 (2004) 215–226.
[10] M.A. Stremler, F.R. Haselton, H. Aref, Designing for chaos: applications of chaotic advection at the microscale, Philos. Trans. Roy. Soc. Lond. A 362 (2004) 1019–1036.
[11] M.A. Stremler, B.A. Cola, A maximum entropy approach to optimal mixing in a pulsed source–sink flow, Phys. Fluids 18 (1) (2006) 011701.
[12] B.A. Cola, D.K. Schaffer, T.S. Fisher, M.A. Stremler, A pulsed source–sink fluid mixing device, J. Microelectromech. Syst. 15 (1) (2006) 259–266.
[13] J.-M. Hertzsch, R. Sturman, S. Wiggins, DNA microarrays: design principles for maximizing chaotic, ergodic mixing, Small 3 (2) (2007) 202–218.
[14] R. Sturman, J.M. Ottino, S. Wiggins, The Mathematical Foundations of Mixing, Cambridge University Press, Cambridge, 2006.
[15] S.W. Jones, H. Aref, Chaotic advection in pulsed source–sink systems, Phys. Fluids 31 (3) (1988) 469–485.
[16] L.M. Milne-Thomson, Theoretical Aerodynamics, Dover, New York, 1958.
[17] Milton Van Dyke, An Album of Fluid Motion, Parabolic Press, Stanford, CA, 1982.
[18] S. Taneda, Visualization of separating stokes flows, J. Phys. Soc. Jpn. 46 (1979) 1935–1942.
[19] Ph. Carrière, Lyapunov spectrum determination from the FEM simulation of a chaotic advecting flow, Int. J. Numer. Meth. Fluids 50 (5) (2006) 555–577.
[20] Jay H. Phelps, Charles L. Tucker III, Lagrangian particle calculations of distributive mixing: limitations and applications, Chem. Eng. Sci. 61 (20) (2006) 6826–6836.
[21] A.J. Lichtenberg, M.A. Lieberman, Regular and Chaotic Dynamics, second ed., Springer, New York, 1992.
[22] L.M. Milne-Thomson, Theoretical Hydrodynamics, fourth ed., Macmillan, 1968.
[23] M. Abramowitz, I.A. Stegun, Handbook of Mathematical Functions, Dover, New York, 1968.